Detection and Localization of Multiple Ships Using Acoustic Vector Sensors on Buoyancy Gliders: Practical Design Considerations and Experimental Verifications

Richard Dreo, Alister Trabattoni, Pietro Stinco, Michele Micheli, Alessandra Tesei

Detection and Localization of Multiple Ships Using Acoustic Vector Sensors on Buoyancy Gliders: Practical Design Considerations and Experimental Verifications

Richard Dreo, Alister Trabattoni, Pietro Stinco, Michele Micheli, and Alessandra Tesei

***Abstract*—Real-time detection of illegal activities in maritime areas, such as drug trafficking or illegal fishing, is a very challenging task. It generally requires important and expensive means (patrol planes, coastguard, or navy ships) to provide an efficient monitoring of large areas. As ships emit noise due to their propulsion (propeller and engines), passive acoustic monitoring can be an effective alternative to accomplish this task, at a reasonable cost. To be efficient, the detection process should be autonomous, run in real-time, and should transmit information within a short period. In this study, we demonstrate the potential of using gliders equipped with a tri-dimensional acoustic vector sensor (AVS) to run a survey mission in total autonomy. Based on the ability of the AVS to measure the direction of arrival of the incoming wave, we develop an embedded and real-time processing chain to detect ships and to cluster detections in a multiple-sources scenario. We also propose a receiver that runs in real time to measure the time difference of arrival (TDOA) if multipath propagation occurs. The sonar contacts are transmitted every 30 s to a command and control (C2) station using an acoustic modem, without interrupting the detection process. The C2 can process the sonar contacts with a tracker for target localization; the article also shows that it is possible to get a good estimate of the source distance by processing the TDOA from multipath propagation. The proposed methods are validated on data recorded during an at-sea experiment in shallow waters.**

***Index Terms*—Acoustic vector sensor (AVS), autonomous underwater vehicles, buoyancy glider, passive acoustic monitoring (PAM).**

I. Introduction

COUNTRIES with a large seaboard and maritime areas are facing the huge challenge of maritime surveillance. To detect suspicious behaviors and illegal threats (i.e., fishery in protected areas, drug trafficking, or chemical pollution at sea), authorities have to deploy heavy and expensive means (i.e., patrol aircraft, navy or coastguard ships, and terrestrial stations) to cover very large areas.

Due to their propeller and/or engines, ships emit noise over a large band of frequencies when they are underway. For this reason, underwater passive acoustic monitoring (PAM), using a network of fixed and mobile sensors, is an interesting approach for the coverage of large areas in a cost-effective way. However, to deal with threats like fast boats carrying drugs, the system must fulfill three conditions: to be autonomous, to work in real time, and to transmit detections in quasi-real-time.

During the past years, the Centre for Maritime Research and Experimentation (CMRE) has been working on the concept of autonomous networks for PAM, with a particular interest in developing and testing long-endurance and silent autonomous unmanned vehicles with passive acoustic capabilities to guarantee covertness and persistent coverage of an area. Such vehicles, transformed into cooperative passive sensing robots, allow the design of long-term passive acoustic surveillance networks with portability, flexibility, and reconfiguration capabilities [1], [2], [3], [4], [5], [6], [7].

Different types of sensorized nodes have been developed in recent years, especially wave gliders, bottom sensors, and buoyancy gliders. The results described in this article were collected using a buoyancy glider, which is a relatively small platform that navigates using buoyancy variations as energy for propulsion, without the need of an engine or a propeller [8].

Initially developed for long-term oceanographic missions with duration of several months, this technology can be used for PAM applications. Gliders with single hydrophones [9], [10], [11] are suitable for measuring wideband ambient noise spectra, without the capability either to estimate the direction of arrival (DOA) of noise sources or to distinguish among noise sources with the same frequency content. Short linear arrays or compact volumetric arrays of hydrophones [12], [13], [14] can provide these capabilities, but only in frequency ranges generally beyond 1 kHz, given the hydrophone spacing, geometrical constraints, and the selected array processing methods. These acoustic payloads are particularly appropriate for acoustic monitoring of fast small- or mid-sized motorboats.

Manuscript received 12 January 2021; revised 7 February 2022, 2 August 2022, and 25 August 2022; accepted 31 August 2022. This work was supported by the NATO Allied Command for Transformation under the Project "Maritime Unmanned Systems for ASW" of the STO-CMRE Programme of Work. *(Corresponding author: Alessandra Tesei.)*

Associate Editor: W. Xu.

Richard Dreo, Pietro Stinco, Michele Micheli, and Alessandra Tesei are with the NATO STO Centre for Maritime Research and Experimentation (CMRE), 19126 La Spezia, Italy (e-mail: richard.dreo@cmre.nato.int; pietro.stinco@cmre.nato.int; michele.micheli@cmre.nato.int; alessandra.tesei@cmre.nato.int).

Alister Trabattoni is with the Institut de Physique du Globe de Paris, Sorbonne Paris Cité, UMR CNRS, 7154 Paris, France (e-mail: trabattoni@ipgp.fr).

Digital Object Identifier 10.1109/JOE.2022.3205647

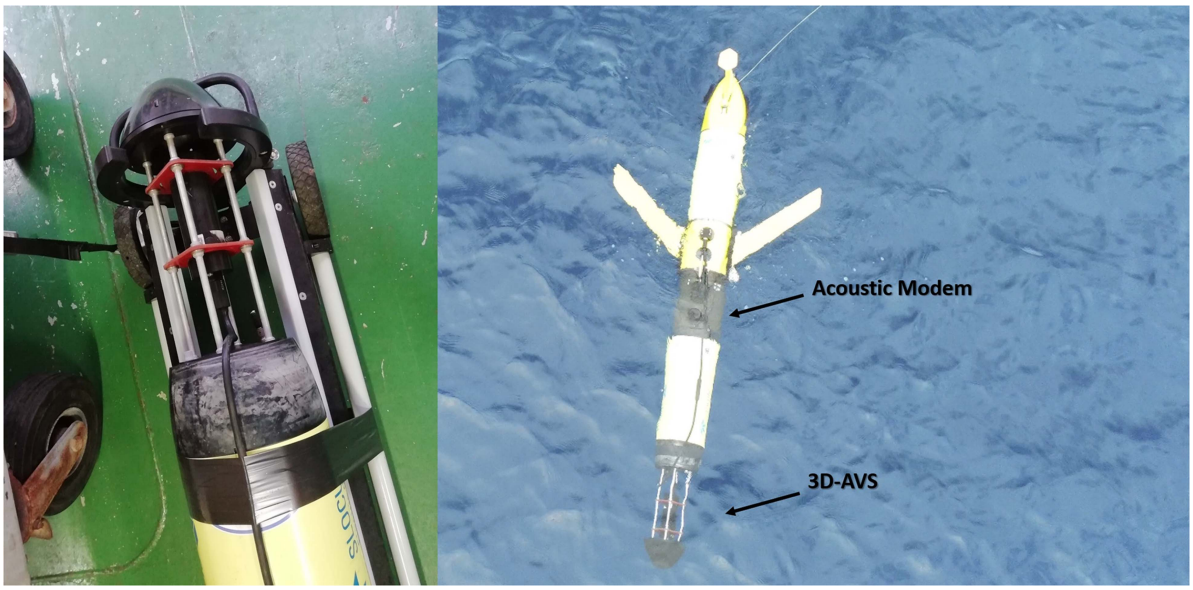

Fig. 1. Picture of the Slocum glider equipped with a 3-D AVS.

In 2018, CMRE started to equip buoyancy gliders with acoustic vector sensors (AVS) of small size that may provide directivity at low frequency despite their limited size, have a certain array gain, and possess receive beampatterns that do not depend on frequency. AVSs are particularly appropriate for PAM of slow and big ships. They achieve the same array gain and beamwidth at frequencies much less than 1 kHz where traditional acoustic pressure sensors would require an array of dimensions incompatible with the glider towing capabilities. The present article builds on the work presented in [2] by proposing two signal processing chains that run in real time on board the glider. The first receiver detects narrowband acoustic signals and extracts their DOA. The second one extracts the time difference of arrival (TDOA) from cepstrum analysis. The TDOA can be processed to estimate the range of wideband noise sources in the presence of multipath with a single, static, or slowly moving, receiver.

In the first section, we will detail the data used in this study and give some useful information about the trial context and the recorded examples. The following two sections will describe the two signal processing chains that run in real time on board the Teledyne Webb Research Slocum glider hosting the 3-D AVS (Fig. 1). These sections will also show the results obtained for the two representative maritime situations.

II. Data Description

The data used for this study were recorded during an at-sea experiment conducted by CMRE in shallow waters off the Italian coast in March 2019 (Fig. 2). The depth in the area was varying between 60 and 350 m. The AVS hosted on the glider was the 3-D GeoSpectrum M20-040 directional hydrophone [15]. This sensor consists of four components: three orthogonal vectors measuring the particle acceleration and one omnidirectional hydrophone measuring the acoustic pressure [16], [18].

Despite its small size (64-mm diameter and 179-mm length), the AVS is capable of measuring the DOA of the incoming acoustic waves in a band extending from 30 Hz up to 3 kHz, with a directivity index of +6 dB [16], [17]. The digital acquisition system on the glider samples the four channels of the AVS at 20 kHz and stores the time series in a succession of 20-s long files. In parallel, an embedded inertial unit records the orientation of the glider in the three dimensions (yaw, pitch, and roll) in real time. The processing unit is an Olimex A20-OLinuXino-Lime2. This CPU processor is an Open Source Hardware embedded ARM Linux Android computer with 1GB RAM Allwinner Dual Core Cortex-A7 A20 (clock: 1.2 GHz). Acoustic data are processed file by file once written on the hard drive disk, meaning that the results are transmitted with nearly 30-s latency.

Running passive acoustic measurements with an AVS requires a high-quality receiving chain and a silent and stable platform. In terms of acquisition system included in the glider acoustic payload, extensive lab tests concluded that the full receiving system has an equivalent input noise comparable to sea state 1.5 [12].

As an underwater platform, the buoyancy glider is one of the most silent mobile underwater vehicles that are currently available, thanks to the lack of any propeller or engine, and to very slow and smooth motion. For most of its mission time, there is no noise generated by any acceleration of the glider or by the motion of any of its mechanical parts. Due to a limited speed and to the geometrical configuration of the sensor integration, the flow noise is negligible. However, an essential process to the glider navigation (i.e., the piston activation allowing the buoyancy change) cannot be avoided and involves 30-s periods of sensor saturation every 3−4 minutes, depending on the desired maximum depth of its navigation. To avoid any false detection, the processing chain is suspended during the piston activation. This process is made possible through an innovative, *ad-hoc*, deep integration of the scientific payload with control system of the commercial platform.

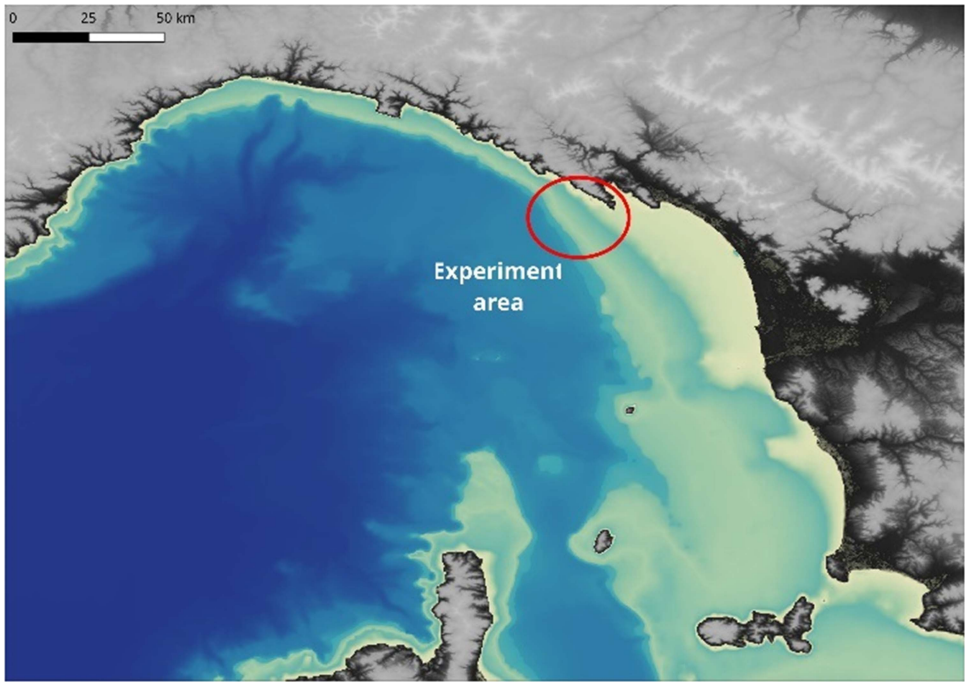

Fig. 2. Area of the experiment conducted in March 2019, off the Italian coasts in front of the Cinque Terre coastline. Sea depth is varying between 60 and 350 m.

In this article, we focus on two data sets, each one including a main acoustic source with known trajectory. In the data set of the first experiment, the main source was a small workboat named Craken. This boat made a helical trajectory (Fig. 3) at a short distance around the glider position and was equipped with a GPS to acquire the position with good accuracy.

In the second data set, the main source was a 125-m long cargo ship named Marfret Niolon with Maritime Mobile Service Identity (MMSI) number 253343000. While crossing the area, the cargo was transmitting the GPS position through the automatic identification system (AIS) which allowed to reconstruct its trajectory with good accuracy (Fig. 4). Both the runs have a duration of about 15 min.

A. *Craken Trajectory*

Fig. 3(a) gives a detailed view of the Craken trajectory, while Fig. 3(b) provides her distance from the glider. In this 15-min run, the Craken turned clockwise around the glider at a short distance ranging from 100 to 500 m, at a speed of 5−6 kn. The consequence is an important azimuth variation rate, up to 30°/minute, and a very high signal-to-noise ratio (SNR).

During this run, several sources of low SNR radiated noise were also present near the glider (more details in Section III). This situation illustrates that the extreme conditions the algorithm must be able to be dealt with in terms of azimuth variation as well as source SNR contrast. Even if not fully representative of a real situation at sea (because of the spiral trajectory), this run is a relevant case to test the robustness of the processing chain. The bottom depth around the glider was 65 m and the mean sound speed was 1508 m/s. The typical yo-yo navigation of the glider, consisting of subsequent diving and climbing phases, is shown in Fig. 3(c); the glider maximum depth during the experiment was 42 m.

B. *Marfret Niolon Trajectory*

The merchant ship Marfret Niolon (MMSI 253343000) is a white target of opportunity that moved near the glider at a distance lower than 3000 m with a closest point of approach (CPA) of about 500 m [distance curve given in Fig. 4(b)]. The ship speed was 12−13 kn. As shown in Fig. 4(a), the trajectory is simple and can be divided into two sections. During the first section, the ship's heading was 103°, while it was 90° during the second section. Numerous multipath propagation features could be observed, providing a good opportunity to illustrate the distance estimation method. The bottom depth in the area was about 75 m. The mean sound speed was 1508 m/s. The glider maximum depth was 32 m [Fig. 4(c)].

III. Detection and Clustering of Multiple Noise Sources

The detection processing chain is based on the ability of a single AVS to provide the DOA of incoming sound waves even in the low-frequency band. To detect and separate automatically different sources, the approach consists in extracting several features from the signal and then applying a clustering algorithm. The intensity vector (presented below) is the base of the processing chain and will be used to compute the different inputs of the clustering algorithm. Due to the instrumental design of the selected AVS, the effective bandwidth of the sensor is 30−3000 Hz. Out of this frequency band, the DOA is either noisy or inconsistent.

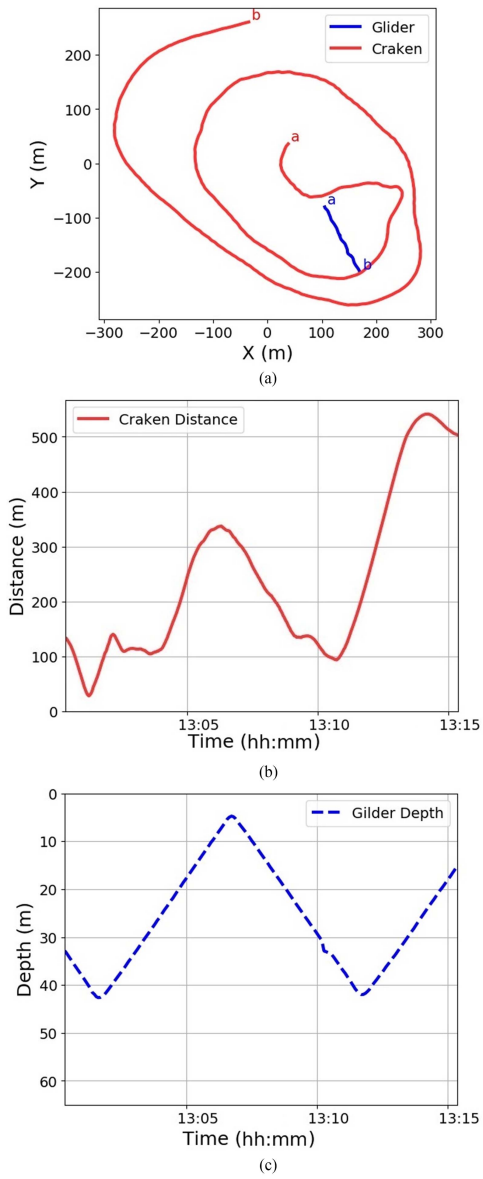

Fig. 3. (a) Craken (red) and Glider (blue) trajectories (in a local tangent plane reference system). The vessel turned clockwise around the glider and remained at a short distance. (b) Craken distance to the Glider. She stayed within a 500-m radius during the experiment. (c) Glider depth during the experiment, cruise speed of 0.37 m/s.

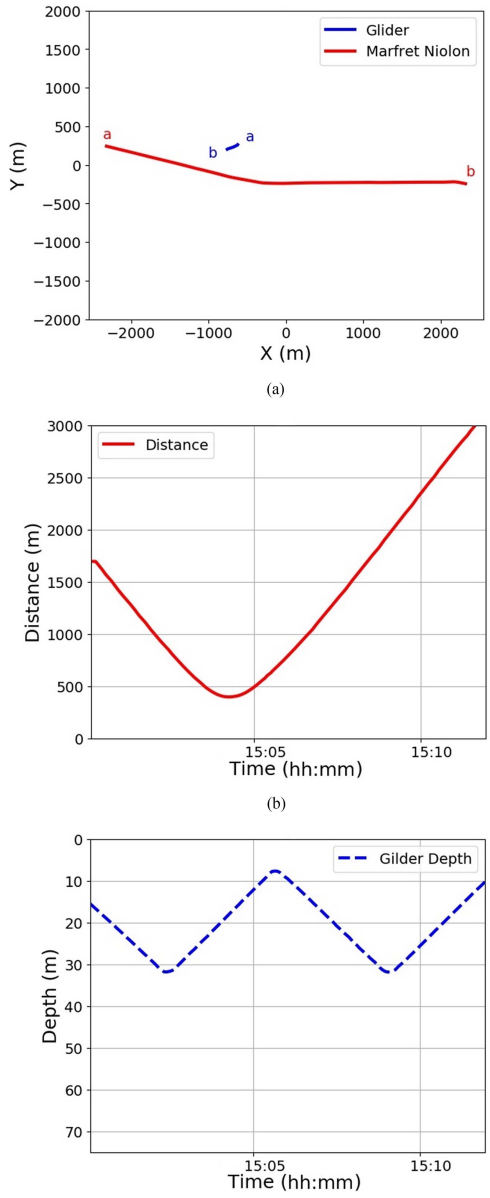

Fig. 4. (a) Marfret Niolon (red) and Glider (blue) trajectories. (b) Distance between the glider and the ship during the time-window of measurement. (c) Glider depth during the experiment, cruise speed of 0.38 m/s.

A. *Intensity Vector*

The first step of the receiver is to compute the short-term Fourier transform of the four signals at the output of the AVS. The resulting time-frequency representations of these signals are noted $S_p(f,t)$ for the acoustic pressure (measured by the omnidirectional pressure sensor) and $S_x(f,t)$, $S_y(f,t)$, and $S_z(f,t)$ for the three orthogonal components, such as

$$\boldsymbol{S}_v(f,t) = [S_x(f,t)S_y(f,t)S_z(f,t)]^T$$

is the time-frequency particle velocity vector. We compute the intensity vector $\boldsymbol{I}(f, t)$ as the real part of the complex intensity vector [2], [19]

$$\boldsymbol{I}\,(f,t) \;= 0.5\mathrm{Re}\left\{S_{\mathrm{p}}\,(f,t)\,\boldsymbol{S}_{\mathrm{v}}^{*}\,(f,t)\right\}. \qquad (1)$$

The spectrogram of the modulus of the intensity vector from 0 to 400 Hz is shown in Fig. 5(a). We can observe several tonals belonging to the Craken (especially the 50 Hz and its harmonics mainly during the first minutes) and other tonals belonging to other remote ships.

Having low and high SNR sources at the same time, this run is a very interesting case to challenge the robustness of the source separation capability of the proposed receiver. In practice, the spectrogram parameters (namely, fast Fourier transform size and overlap) must be chosen in accordance with the CPU capabilities, taking into account that we are interested in continuous, narrowband signals. Preserving a good frequency accuracy is important to separate closed-by tonals with different SNRs.

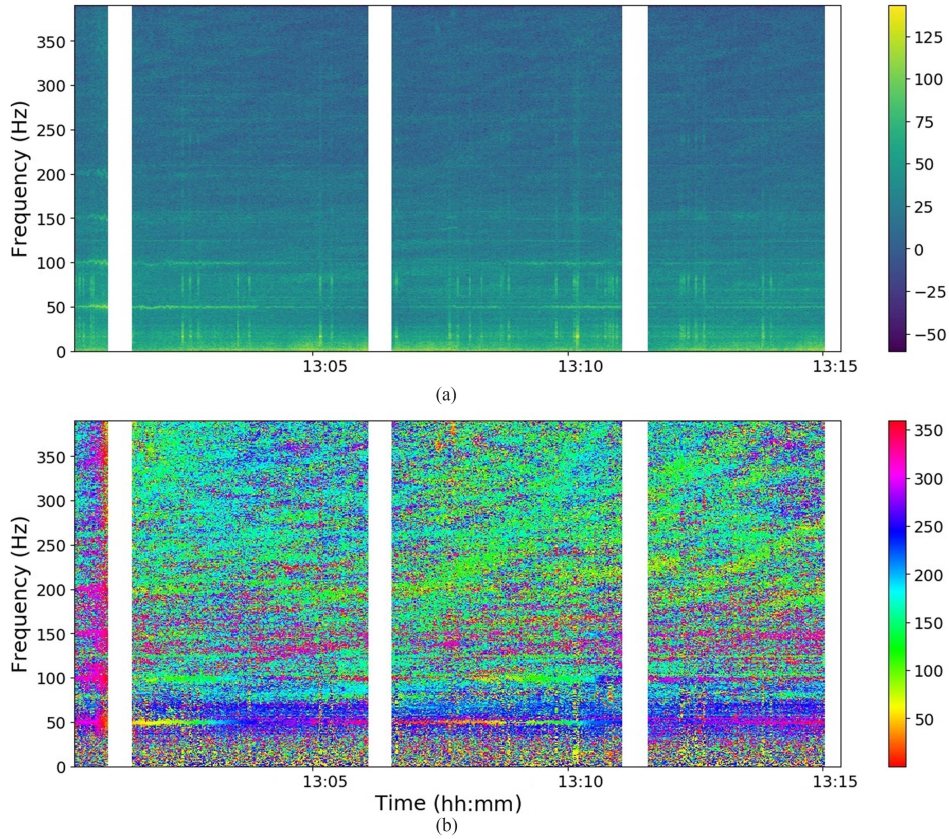

Fig. 5. (a) Spectrogram of the modulus of the intensity vector [dB re pW/m^2/Hz] with Craken data. Tonal frequencies belonging to the Craken (50 Hz and harmonics) and several ships of various SNRs are visible. White vertical bands correspond to the activation periods of the glider piston, removed from the processing. Color scale indicates the signal level in dB. (b) Azigram, i.e., measured azimuth in the time-frequency domain. Color scale indicates the azimuth in degrees from 0 to 360 rotating clockwise from North. Note that the 50-Hz tonal belonging to the Craken workboat is changing azimuth color according to the spiral path around the glider. The same azimuthal variation can be observed in the harmonics at 100, 150, and 200 Hz. Other ships are present but not easily distinguishable by visual inspection in this plot [more visible in Fig. 6(a)].

In this particular case, there is a 50-Hz tonal with high SNR belonging to the Craken very close in frequency to a 54-Hz tonal belonging to the ship with MMSI 247112070. Additionally, a third tonal at 56 Hz is visible.

The origin of the latter one is not clear, since the only ship reporting her position in this sector is the one with MMSI 247112070. As the 54- and 56-Hz frequencies have slightly different azimuthal curves and different times of appearance (even if sometimes visible simultaneously), they probably belong to different ships.

B. Direction of Arrival

From the intensity vector $\boldsymbol{I}(f, t)$, it is possible to compute the DOA, that is azimuth (θ) and elevation (ξ) of an incoming acoustic wave with the following equations [2]:

$$\theta(f,t) = atan\left(I_x(f,t)/I_y(f,t)\right) \quad (2)$$

$$\xi(f,t) = atan\left(\left(I_x^2(f,t) + I_y^2(f,t)\right)^{1/2}/I_z(f,t)\right). \quad (3)$$

Here, $I_x(f, t)$, $I_y(f, t)$, and $I_z(f, t)$ are the spectrograms of the North-East-Down components of the intensity vector after a 3-D rotation using the roll, pitch, and yaw measurements from the inertial unit of the glider.

Fig. 5(b) shows a time-frequency representation of the measured azimuth called azigram [2], [3], [20]. The color-coding corresponds to the azimuth, rotating positive clockwise from North. As the experiment took place in shallow waters, the elevation mainly corresponds to the horizontal plane and does not provide useful information for distant sources. In practice, in the first studied example, the elevation carries information only when the observer-Craken distance is less than 200 m. For this reason, the elevation plots are not shown in this article.

C. Tonal Extraction Procedure

The azigram is a view of the wideband signal DOA reaching the AVS. Each pixel can be seen as the main DOA (i.e., main source) at a time t for a frequency bin f. At this point, it is difficult to discriminate among several sources, especially when low SNR sources (distant or weak) are "mixed" with a high SNR source.

The receiver running on-board the glider is designed to detect the narrowband tones generated by the propellers and the engines of sea vessels; therefore, it is also useful to separate the wideband from the narrowband components of the signal. This is done by the filter described in this section.

Fig. 5(b) shows the azigram recorded when the Craken was making a spiral pattern around the glider at a very short distance (details of the trajectory in Fig. 3). The tonal at 50 Hz is representative of the Craken azimuth variation. We see that the azimuth is continuously changing at that frequency, in accordance with the spiral trajectory. In this case, it is quite challenging to immediately identify the number of sources present on the azigram. Anyhow, it is possible to notice that several tonals show different azimuth variations, meaning that several sources are simultaneously present.

Due to their propeller and/or engines, small and big boats generate narrowband signatures mainly visible in the low-frequency band. A way to facilitate the source discrimination is to focus on these tonals and to reject the main part of the wideband signal which does not carry additional information in terms of DOA. The choice was made to focus on the $0-400$ Hz frequency band, with the effect to reduce the amount of data to compute without losing any frequency accuracy, but one can notice that it is still possible to apply the same process on the full frequency band.

The extraction of the tonals is performed using a constant false alarm rate (CFAR) detector [21] on the modulus of the intensity vector. The CFAR detector normalizes each time-frequency point of the spectrogram with a local estimate of the background noise power using a bidimensional median filter on the reference cells close to the cell under test. This normalization corresponds to a local estimate of the SNR which is compared to a constant threshold for detection.

The number of reference cells is a compromise between the time and frequency resolutions and the glider CPU capabilities. Here, a 11×11 points kernel was applied. The bins of the spectrogram having a value above a given threshold are used to build a transparency mask. Increasing the threshold will improve the effectiveness of this tonal filtering step, with the risk of losing an important part of the useful information. In our example, the threshold is empirically set to 19 dB. This high value of the threshold can be predicted with simulations as described in following sections, but it is mainly dictated by the fact that in shallow and coastal waters, there are usually several noise sources and a low value of the threshold risk to saturate the clustering algorithm with an enormous amount of detected signals. When the objective is to detect very quite targets, a lower value of the threshold is desired such as a threshold of 6 dB.

Depending on the threshold, wideband components not corresponding to ships' tonals can remain, as well as transient signals. To reject those features, the following step consists in keeping only the bin groups having a duration above 2 s. The expected effect is to reject the undesired short-term transients, and also the time-frequency bins corresponding to the wideband noise, i.e., the bin groups without consistency in the time domain. The obtained transparency mask is applied to both the spectrogram and the azigram.

Fig. 6(a) shows the azigram obtained after the tonal extraction procedure on the Craken recording. The number of informative points is dramatically reduced (crucial to avoid the overload of the clustering algorithm) without losing the useful information.

D. Clustering

The outputs of the previous steps are the filtered spectrogram and azigram, meaning that we have the information about the amplitude and azimuth of the selected time-frequency bins.

The clustering process is made by a density-based spatial clustering of applications with noise (DBSCAN) algorithm [22] applied to time windows of 20 s. The DBSCAN aims at associating the time-frequency bins based on the frequency-amplitude-azimuth continuity over time. It means that we use the algorithm in a way that it will extract tonals, without grouping them by source (one ship can radiate several frequencies or tonals). The reason of this choice is that working on 20 s windows does not provide enough information on the azimuth variations along the time axis to merge the detected frequencies as a unique source, especially when they are in the same azimuth. Increasing the clustering time-widow to $5-10$ min can solve this problem but with the consequence of increasing the number of points to cluster and, hence, with the critical risk to overload the CPU.

The input values of the DBSCAN are the frequency, the amplitude, and the azimuth of each detected bin at the output of the transparency mask. As we intend to cluster variables with different units, a previous standardization step is necessary to adapt the different scales. Note that the time information is not provided to the DBSCAN algorithm because the observation time window is small (as said, 20 s of duration) and, in this time frame, it is assumed that only one target is emitting at the same frequency in the same azimuth. The probability that two or more targets are emitting the same tone from the same DOA in the same time window of 20 s is very low. Finally, all the bins that do not belong to a cluster are considered as clutter and discarded.

E. Transmission to the Gateway

The output of the processing chain for each file is composed of a list of bin clusters grouped by frequencies. At this point, the amount of data is too large to be transmitted to the topside through the ultra short baseline (USBL) modem. A simple compressing step is done for each tonal by averaging the cluster azimuths. For each 20-s window and for each detected tonal, three equally spaced time-azimuth values are processed and transmitted to the gateway. It allows a correct reconstruction of the different curves on the topside (i.e., the mother ship) and gives an overview of the situation encountered by the glider.

F. Performance With Real Data

As discussed, Fig 6(b) shows the output of the detection and clustering algorithm. A summary of the detection results and related experimental conditions is given in Table I. The table shows the performance in terms of time on target, i.e., the percentage of time over which a tone has been detected during the experiment. The association between the detections and the noise sources is based on the AIS data. A total of 12 ships transmitted their positions in a 30×30 km^2 area around the glider. Their positions are reported in Fig. 7(a), while Fig. 7(b) shows their distances from the glider.

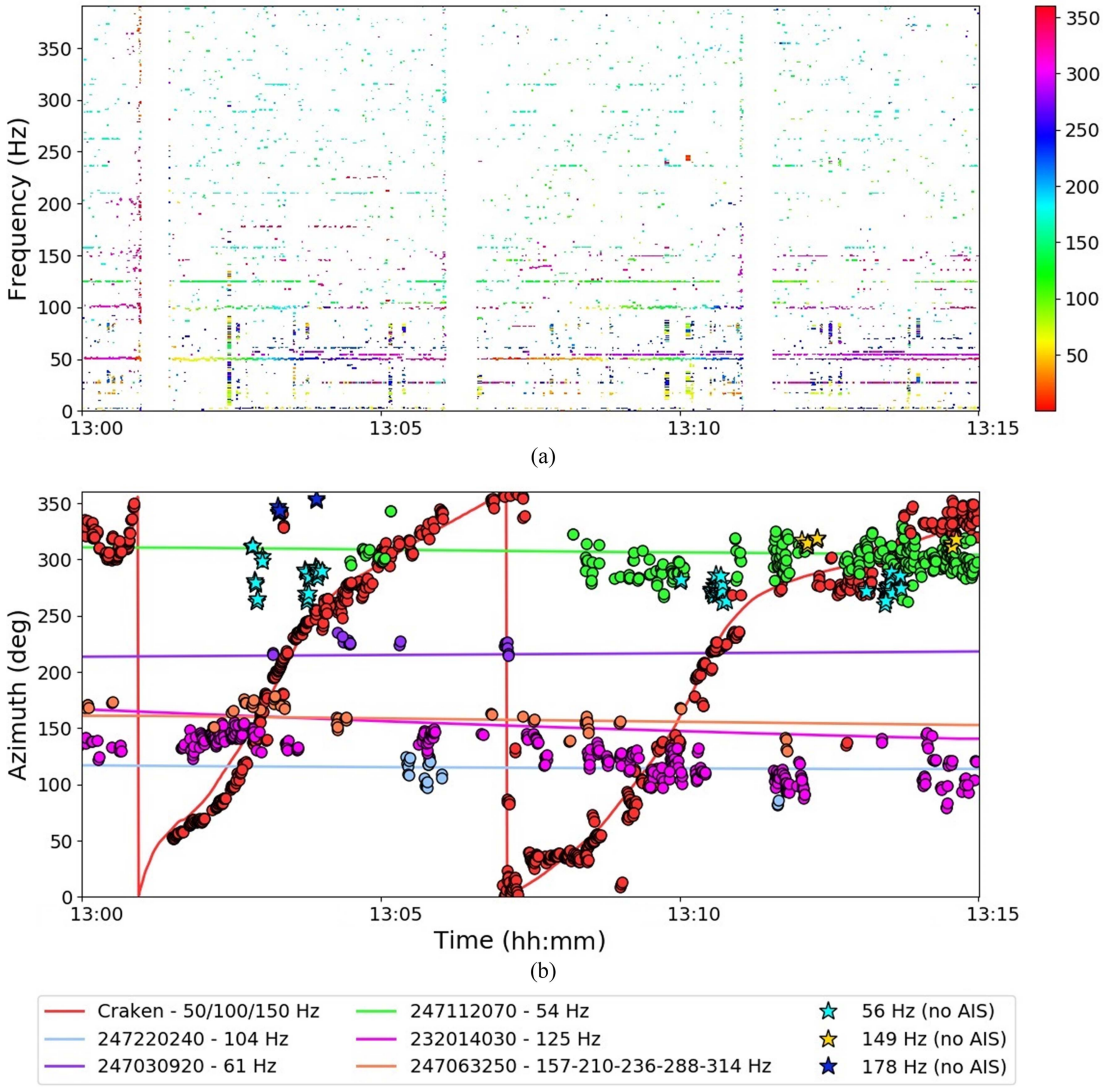

Fig. 6. (a) Narrowband azigram. Background noise is efficiently filtered out and only the DOAs are kept in regions where the SNR is higher than a given threshold for at least 2 s. (b) DOA of the contacts at the output of the clustering algorithms compared with ground truth from AIS data. Circles with the same color indicate contacts labeled as belonging to the same noise source, and the same color is used for the ground truth. Two sources identified by the clustering algorithm do not correspond to any AIS in the vicinity and might correspond to ships not equipped with AIS (plotted with stars).

The ships detected by the processing chain are plotted in colored lines, while the missed detections are plotted in black dashed lines. All the black trajectories belong to 15−20 m long fishing boats, having speeds slower than 3 kn. The detected ships are four fishing boats (MMSI: 247112070, 247030920, 247220240, and 247063250) and one pleasure craft (MMSI 232014030). Note that due to the coast proximity, there is only one ship (247112070) reported in the North sector of the glider. The distance of the detected sources is up to 25 km, which is consistent with the performance predicted with Monte Carlo runs that will be discussed in the following subsection.

As previously mentioned, there are also three detected targets that cannot be linked with AIS data. First, a 56-Hz tonal is detected in the same sector as the 54 Hz belonging to 247112070 but with a much lower SNR. Additionally, the times of appearance of the two tonals are too different to belong to the same ship. The second one is the 178-Hz tonal detected from 13:03 to 13:05 at azimuth 350° [corresponding to red in the colorbar of Fig. 6(a)]. The last detected target with no AIS is the 149-Hz tonal at azimuth 310° observed during the last 3 min of run.

The three 56-, 149-, and 178-Hz detections are relevant, even if no corresponding ground truth in the AIS data can be found. In coastal areas like this, such a situation can often occur due to the presence of small pleasure boats for which AIS reporting is not mandatory. Instead, in high seas, where practically all ships have to report their positions due to their tonnage, this is the typical kind of situation that could interest authorities, as it could correspond to a ship hiding its position during illegal activities.

Fig. 8 provides the results of the detection process applied on the second case study. Here, only the Marfret Niolon ship is visible on the azigram [Fig. 8(a)], with colors varying from purple to green. Many tonals corresponding to the propulsion Diesel

TABLE I
DETECTED SOURCES AND THEIR CORRESPONDING GROUND TRUTH INFORMATION EXTRACTED FROM THE AIS DATA

MMSI	Speed (kn) mean [min - max]	Distance (km) [start - end]	Freq (Hz)	Time on target (%)
Craken	5.3 [5.0 – 6.1]	[0.05 - 0.5]	50 100	100% 60%
247112070	2.4 [2.0 - 3.2]	[2.9 - 2.0]	54	70%
247030920	2.6 [2.2 – 3.2]	[12.3 – 13.1]	61	35%
247220240	2.8 [0.6 - 3.6]	[8.6 - 9.4]	104	20%
232014030	16.6 [14.6 - 17.3]	[12.5 - 16.0]	125	80%
247063250	9.7 [8.50 - 10.6]	[28.5 - 28.1]	157 236 288 314	50% 25% 25% 25%
Unknown	/	/	56	10%
Unknown	/	/	149	20%
Unknown	/	/	178	30%

The percentage of detection time is given for each detected frequency. The "deaf" periods due to the piston activation are not taken into account for the percentage calculations.

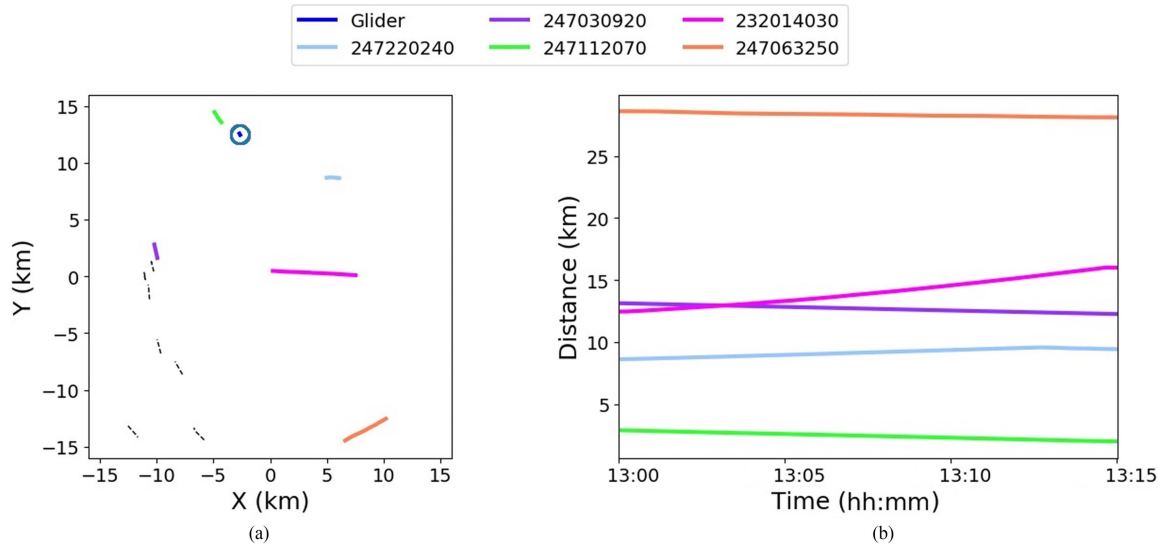

(a) (b)

Fig. 7. (a) Ship positions in the neighborhood of the glider location (AIS data) while the Craken workboat was making a spiral trajectory (in the blue circle). The detected ships are plotted in colored lines; black dashed lines represent ships not detected by the algorithm. (b) Distances of the detected ships from the glider observer.

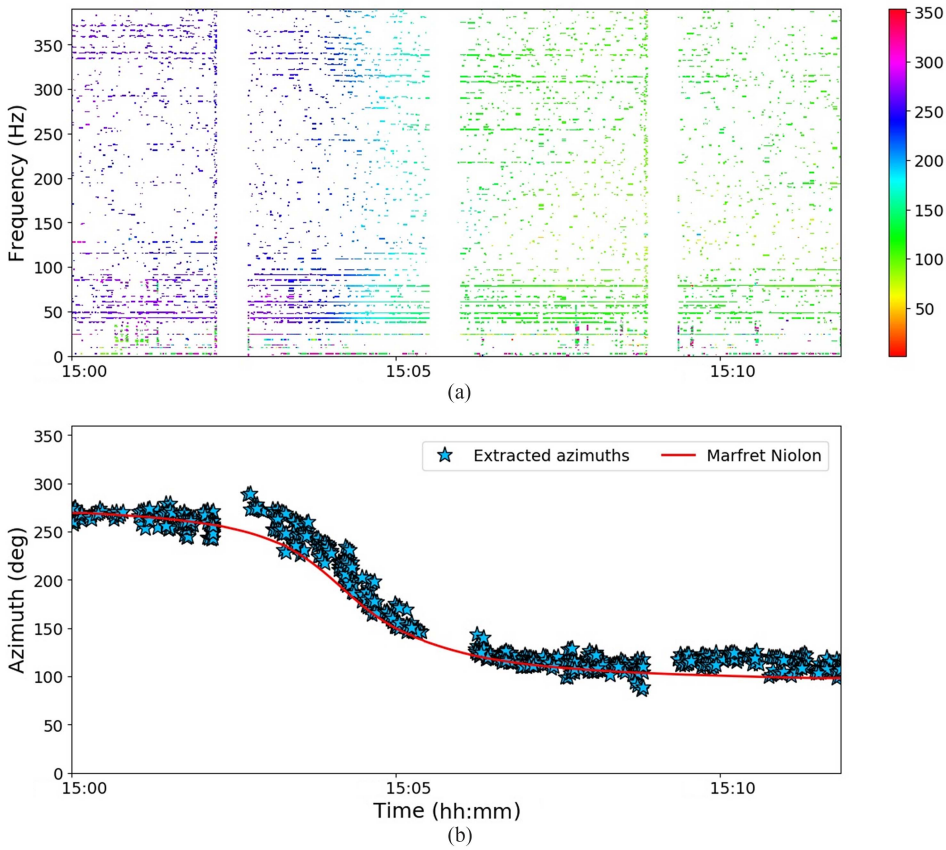

Fig. 8. (a) Narrowband azigram of the Marfret Niolon case. Many frequencies belonging to the propulsion Diesel engines are visible. (b) Extracted contacts, all of them belong to the ship Marfret Niolon and very well match the AIS ground truth.

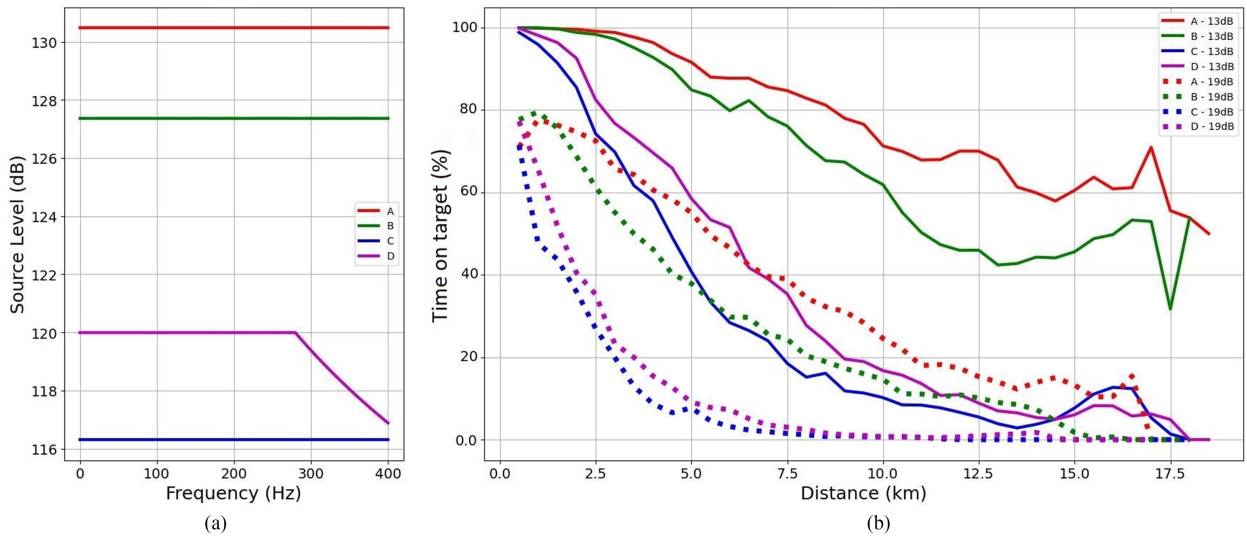

Fig. 9. Performance curves of the detection chain processed with Monte Carlo simulations. (a) Wideband spectrum of the four considered categories A, B, C, and D. (b) Time on target as a function of the source distance for two different threshold values (13 and 19 dB).

engines are visible, as well as remaining wideband component. The 53 frequencies detected by the algorithm during the 12-min period are plotted on Fig. 9(b) as a unique source to preserve visibility. The extracted azimuths [Fig. 8(a)] are consistent with the ground truth issued from the ship AIS (red line).

G. *Performance Evaluation*

The performance of the detection and clustering receiver has been also evaluated by Monte Carlo runs simulating the same environment of the real-data analyzed in this article.

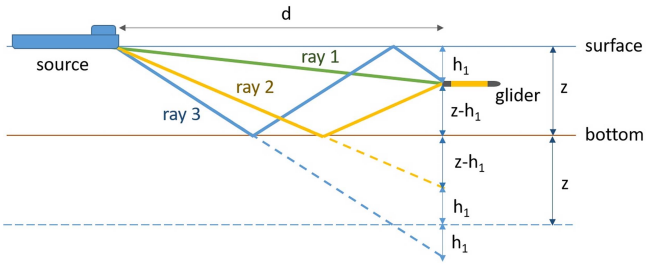

Fig. 10. Multipath propagation cases. Case 1: TDOA between ray 1 (direct) and ray 2 (1-bottom reflection path). Case 2: TDOA between ray 1 and ray 3 (1-bottom/1-surface reflection path). Case 3: TDOA between ray 2 and ray 3.

In the simulation, consisting of 500 runs, we assumed low traffic density, wave height of 2 m, and sea current of 0.5 m/s. The duration of each Monte Carlo was 30 min and we assumed that four targets were passing by the receiver at different distances. The spectral characteristics and trajectories of the targets were set as follows:

1) wideband level chosen in one of the four categories (A, B, C, D) corresponding to different source levels plotted in Fig. 9(a);
2) 1−4 narrowband frequencies having a signal excess of 20−30 dB over the wideband spectrum;
3) CPA between 500 and 10 000 m;
4) heading between 0° and 360°.

The transmission loss of each noise source has been obtained using the shallow water propagation model described in [23] and [24].

Fig. 9(b) shows the performance of the detector in terms of time on target of the four categories as a function of the distance and for two values of the thresholds (13 and 19 dB).

The maximum detection range of categories C and D is about 9 km with the threshold of 19 dB (dashed lines) versus 17 km with the 13 dB threshold. In the case of the categories A and B, the time on target of the 19-dB threshold falls to zero at about 17 km, while it is still 50% for the 13-dB threshold. This is consistent with the empirical results obtained with real data and reported in Table I.

The lower the threshold is, the higher is the time on target; however, the larger is the number of bins to be processed by the clustering algorithm. The threshold value of 19 dB is the good compromise for the computational capability of the small CPU installed on the glider since with lower values of the threshold, the computational time may become a significant limitation due to the higher number of bins to cluster.

IV. Target Range Estimation from Multipath Propagation

When propagating through the marine environment, the acoustic waves can follow several paths besides the direct path connecting source and observer. If the source level is high enough and depending on the sound-speed profile, the sea roughness, and the geoacoustic properties of the sea bottom, these acoustic waves can be recorded by the receiver after multiple reflections on both the bottom and the sea surface.

Due to their geometry, each path has a different length so that the traveling times between the source and the receiver are different, even under the hypothesis of constant sound speed. Consequently, the phase difference generates constructive or destructive interference between the acoustic waves and modifies the received level of the wideband signal of the source. If the acoustic signals has a significant wideband component, this phenomenon, known as the Lloyd's mirror effect, is materialized by typical fringes on the spectrogram [25], [26]. From this particular effect, it is possible to measure the TDOA between the main different paths [27], [28].

The wideband receiver described in this section runs in real time on board the glider to measure the TDOAs through cepstrum analysis [20], [29], [30], [31]. The cepstrum of a signal measured in a certain time window is defined as the inverse Fourier transform of its logarithmic spectrum and highlights periodicities of the measured spectrogram. As for the spectrogram, we can get a cepstrogram by computing the cepstrum of the signal over adjacent (or overlapped) time windows. In our study, the cepstrum is obtained from the intensity vector $\boldsymbol{I}(f)$:

$$C\ (\tau) = F^{-1}\left(\log \|\boldsymbol{I}\,(f)\|^2\right). \tag{4}$$

In the case of an acoustic source, it will provide two important pieces of information: 1) a time-invariant component, corresponding to the source term (i.e., the link between the fundamental frequencies and their harmonics); 2) a time-varying component corresponding to the propagation term, which is the consequence of the multipath propagation. To extract this propagation term, we apply a singular value decomposition (SVD) clutter filtering on the cepstrogram, as described in [20] and [32]. After this SVD filtering step, we consider that a significant value in the remaining quefrencies will correspond to a TDOA between two paths.

When measuring the TDOA on the cepstrogram, it is not possible to know immediately which are the paths involved. However, an important feature to help in this identification is that, if the surface and bottom are ideal soft and hard boundaries, respectively, an odd number of reflections on the sea surface leads to a negative amplitude on the cepstrogram, while an even number of reflections on the sea surface will generate a positive amplitude [32]. This will be considered in the following subsections.

A. Multipath Propagation Cases

The measured TDOAs on the cepstrogram depend on the different paths involved. In this study, to demonstrate the feasibility of the distance estimation process, we first generalize the equation of the TDOA between two rays with an arbitrary number of reflections on the sea surface and sea bottom; then we focus on the three most simple and frequent cases shown in Fig 10.

Each case is the combination of two among three dominant propagation paths: the first path is the direct ray, reaching the glider without any bottom or surface reflection; the second has

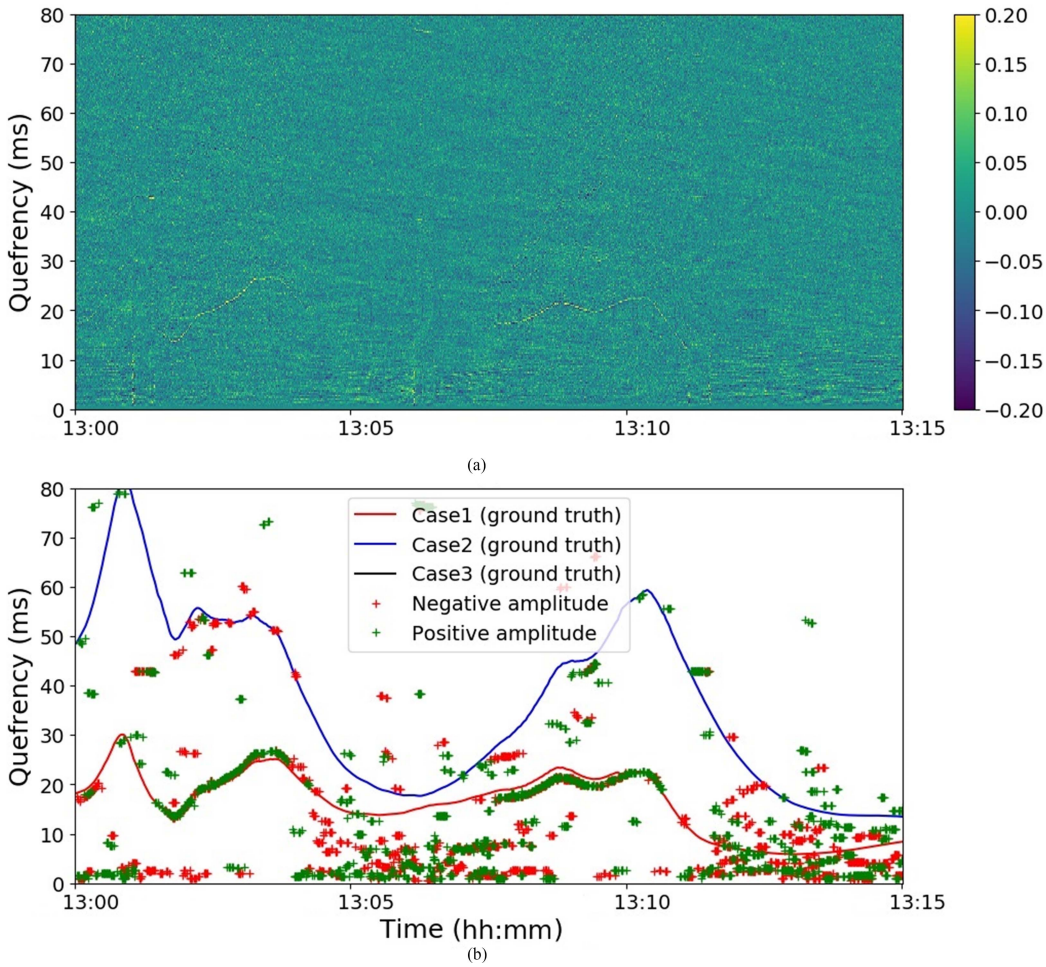

Fig. 11. (a) Cepstrogram of the Craken data set. The thin and yellow positive peak of the cepstrum corresponds to the TDOA of case 1 propagation model. The measured cepstrum peak is varying between 12 and 30 ms and visible from 13:02 to 13:12. (b) Extracted TDOA from the cepstrogram, compared to the ground truth curves. Green crosses correspond to positive peaks of the cepstrum and red crosses are negative peaks of the cepstrum.

one reflection on the bottom; the third has one reflection on the bottom and one on the sea surface.

We consider the isorays environmental model which assumes an isospeed sound-speed profile and calculates expected TDOAs by means of the mirror (or image) method. This is a simple approach that, given the relative short ranges, generally provides a small error between the expected and the measured TDOAs and allows reversing the target distance approximation in closed form.

In the most general case, assuming that the source is at the sea surface at a distance d from the glider, knowing the sound speed (s), that is assumed constant in range and depth and indicating with z the bottom depth and with h_1 the glider depth, the TDOA between two paths can be considered as the difference between the times of arrival (TOA) of the two considered rays, i.e.,

$$t = \frac{1}{s}\sqrt{(2N_b z + k h_1)^2 + d^2} \tag{5}$$

where

$$k = 2\,(N_s - N_b) + 1 \tag{6}$$

and N_s and N_b are, respectively, the number of surface and bottom reflections of the considered ray.

The generalized function of the TDOA between two rays is then obtained by

$$\Delta t = t_2 - t_1 = \frac{1}{s}\left[\sqrt{(2N_{b2} z + k_2 h_1)^2 + d^2} - \sqrt{(2N_{b1} z + k_1 h_1)^2 + d^2}\right] \tag{7}$$

with

$$\begin{aligned} k_1 &= 2\,(N_{s1} - N_{b1}) + 1 \quad \text{for ray 1} \\ k_2 &= 2\,(N_{s2} - N_{b2}) + 1 \quad \text{for ray 2.} \end{aligned}$$

If $d \gg (2N_{b1} z + k_1 h_1)$, using the first-order Maclaurin approximation, for ray 1, we get

$$\sqrt{(2N_{b1} z + k_1 h_1)^2 + d^2} \approx d + \frac{(2N_{b1} z + k_1 h_1)^2}{2d} \tag{8}$$

and for ray2

$$\sqrt{(2N_{b2} z + k_2 h_1)^2 + d^2} \approx d + \frac{(2N_{b2} z + k_2 h_1)^2}{2d}. \tag{9}$$

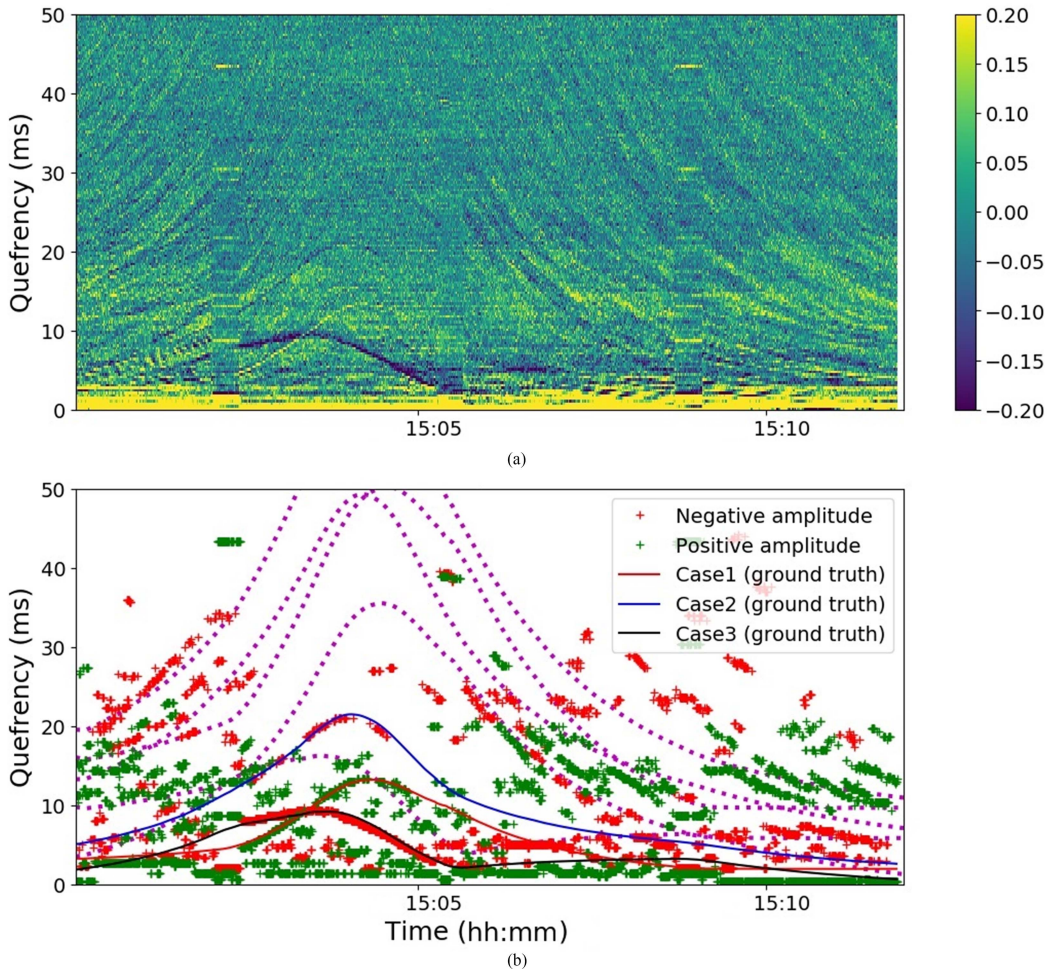

Fig. 12. (a) Cepstrogram of the Marfret Niolon data set. The Lloyd's mirror effect appears during the whole period. The CPA occurs at 15:04. The three main multipath effects are visible from 15:02 to 15:05. One is positive (yellow), while the two others are negative (dark). (b) Red crosses are the extracted TDOA with a negative amplitude in the cepstrum, while positive amplitudes are plotted with green crosses. The ground truth corresponding to the three simple multipath cases are plotted in red, blue, and black lines. Note the good match between the extracted data and the ground truth. Other path combinations are visible at higher quefrencies, and the expected corresponding TDOA are plotted in magenta dotted lines.

The final expression of the distance estimate for a source close to the surface is given by

$$d = \frac{4\left(N_{b2}^2 - N_{b1}^2\right) z^2 + \left(k_2^2 - k_1^2\right) h_1^2 + 4\left(N_{b2}k_2 - N_{b1}k_1\right) z h_1}{2s\Delta t} . \tag{10}$$

Referring to the three most frequent cases shown in Fig. 10, Case 1 is the TDOA between ray 1 (the direct path) and ray 2 (1-bottom reflection path). In this case, there are no sea-surface reflections, and, hence, the amplitude on the cepstrogram will be positive.

Using the approximation in (10), the resulting distance is given by

$$d = \frac{2z^2 - 2zh_1}{s\Delta t} . \tag{11}$$

The approximation is valid when the target distance is much larger than the bottom depth, which is often the case in shallow water environments.

Case 2 is the TDOA between ray 1 and ray 3 (the 1-bottom/1-surface reflection path). Having an odd number of surface reflection will lead to a negative amplitude in the cepstrogram.

Using (10), the distance can be approximated as

$$d = \frac{2z^2 + 2zh_1}{s\Delta t} . \tag{12}$$

Case 3 corresponds to the TDOA between ray 2 and ray 3 in Fig. 10. In this case, the approximation of the distance is given by

$$d = \frac{4zh_1}{s\Delta t} . \tag{13}$$

Fig. 11(a) shows the cepstrogram (after the SVD filtering step) of the Craken example. The interesting quefrency corresponds to the thin and yellow cepstum line varying between 12 and 30 ms from the beginning of the run up to 13:12. The yellow color means that the cepstrum has a positive amplitude and is consequently related to an even number of surface reflections. As will be clear in the following plots, this positive peak corresponds

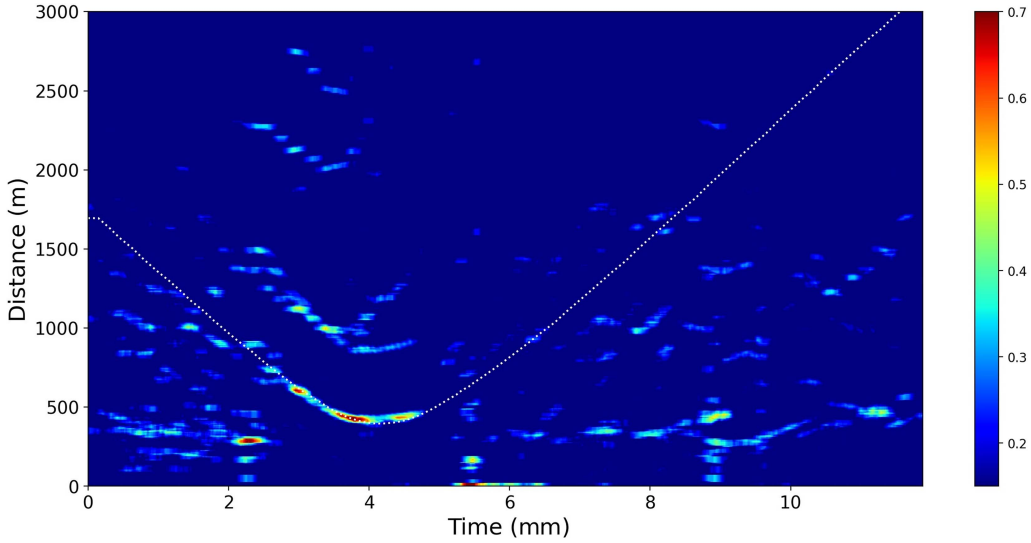

Fig. 13. View of distance probability matrix obtained after inversion of the extracted TDOA. Consistent distances are found before the CPA (T_0 to $T_0 + 2$ mn) and around the CPA ($T_0 + 2$ to $T_0 + 5$ mn). After $T_0 + 5$ mn, the good detections are rare. The dotted white curve is the ground truth.

to the propagation case 1 described above. The peaks of the cepstrum and the expected values of the TDOA based on the known position of the target and the assumed propagation paths are shown in Fig. 11(b). As can be seen, there is a very good match between the measured and the expected TDOAs.

Fig. 12(a) is the cepstrogram obtained with the Marfret Niolon data set. Due to the high source level and the relatively small distance, a high number of paths reached the sensor with a sufficient sound energy, generating many fringes on the cepstrogram. The three main visible curves, corresponding to the three propagation cases can be observed from 15:01 to 15:06. Case 1 is the yellow (positive) curve between 3 and 12 ms, case 2 is the thin dark (negative) curve between 10 and 20 ms, and case 3 is the strong dark (negative) curve under 10 ms. The expected TDOA curves based on the ground truth and the assumed propagation models are shown in Fig. 12(b). The figure also shows in magenta the expected TDOA of higher order propagation models. From the plot, it is possible to appreciate the good match between the expected and measured TDOA.

B. TDOA Extraction

The extraction consists in picking up for each time step, the local maxima and minima of the SVD-filtered cepstrogram that are the potential TDOAs between the different paths generated by the main source. These peaks are extracted by processing the modulus of the cepstrum but taking also into account the original sign of the cepstrum to be evaluated if the number of reflections on the sea surface is even or odd.

To that purpose, we first compute an estimate of the background noise with a 2-D median filter (as for the spectrogram in the azimuthal estimation chain) and then we select only the local maxima with an amplitude larger than the local estimate of the background noise. A peculiarity of the cepstrogram is that around the CPA, where the fringes of the spectrum are very close to each other and the spectrum varies very fast, the TDOAs are well separated. In this case, it is very rare to observe very close peaks in the quefrency domain and a bin of high amplitude is not supposed to have very close neighbors. Hence, we will take advantage of this peculiarity to apply a second filtering level to remove the less significant quefrencies. To do so, each peak of the cepstrum is convolved by a Gaussian curve, leading to a smooth envelope-like curve. Peaks that are under this envelope are then rejected. As a consequence, all the values with low amplitude in the neighborhood of a high amplitude peak are rejected. After this step, few regions of the cepstrogram with no significant peak will not be properly cleaned and sparse clusters can remain. To finalize the process and remove these noisy parts, once again, we apply the DBSCAN clustering algorithm on the remaining values. In practice, this clustering process runs on a 3-min sliding time window to improve noise rejection. Increasing the time window size here does not overload the CPU because the number of points to cluster is small compared to the azimuth estimate case. All the time-quefrency bins that do not belong to a cluster are considered as noise and removed.

C. Results of the Distance Estimate Chain

Fig. 11(b) shows the TDOAs extracted by the distance estimate chain for the Craken case. They are shown as red and green crosses corresponding to negative and positive amplitudes, respectively.

The expected TDOA (cases 1 and 2) obtained from the ground truth are the red and blue curves. When the wideband noise from the Craken is high and TDOAs are visible, we notice a very good comparison with the ground truth. Elsewhere, we can see that there are many quefrencies under 10 ms, The origin of these quefrencies is not clear as it may be either simply noise, or the multipath effect from the ship 247112070, which is about 3-km away from the glider and also shows a wideband contribution. Due to the distance, only considering more reflections than the three cases included in this study might give more insight in this data analysis.

Fig. 12(b) provides the same outputs for the second study case. In this recording, the Marfret Niolon ship is the only visible source, with a high source level generating a strong multipath propagation. We can see the comparison between the output of the distance processing chain and the expected TDOA of the different multipath. We see that below 700−1000 m (i.e., about 10 times the bottom depth), the comparison between the extracted features and the ground truth is very good, but at higher distances, the three simple cases are not visible anymore. To get distance information at a longer range, where a more complex propagation structure occurs, we need to consider other cases given by the generalized function [see (10)]. We can see that these cases (plots in magenta) were detected by the algorithm from 15:00 to 15:03 (10−30 ms) and after 15:06 (10−30 ms).

The TDOAs are sent to command and control with the acoustic modem and processed by the tracker for target localization. The inversion of the measured TDOAs is not performed in real time by the receiver on board the glider; however, Fig. 13 shows the probability matrix of the range obtained by inverting the TDOA measurements to demonstrate the potential of these measurements for target localization. Fig. 13 shows the probability matrix of the distance during the Marfret Niolon time window. To build this view, for each considered case, we reversed the measured TDOA to get the associated distance (respecting the negative/positive quefrency principle). The result is stored in a time/distance layer, where the time−distance bin is set to one when returned by the inversion function; otherwise, it is set to zero. When all the cases are processed, a smoothing filter with a kernel size depending on the time−distance resolutions (here 11×11) is applied to all the layers. Finally, the layers are added elementwise to get the final probability matrix shown in Fig. 13 and compared with the ground truth (white dotted line). Before and after the CPA (time 0−2 min and time larger than 5 min), several detections corresponding to the correct source distance exist, even if not the most probable. From 2 to 5 min (i.e., close to the CPA) the most probable solution is clearly corresponding to the correct source position.

V. Conclusion

This article describes the potential of using gliders equipped with AVSs to perform autonomous PAM of an area in real time. Two processing chains were developed to that purpose. The first one, dedicated to the source detection, takes advantage of the AVS's ability to measure the DOA of the incoming waves to separate the different sources and to provide their azimuthal curves. The target detection range with a single AVS is of the order of 10 km; this result with real data is in agreement with the performance predicted with Monte Carlo runs, also presented in this article. The second chain, exploiting the multipathing of waves in the water column, can extract the TDOA between the different paths of a wideband source, which can be directly related to the distance.

With respect to bearing-only trackers that can give a sufficiently accurate target range estimate, if the bearing rate is sufficiently high during a relative long observation time window, the TDOA method described in this article can provide target range estimates with sufficiently high precision even with very short observation time windows.

Future work will aim at combining the two processing chains in a tracking algorithm to provide an efficient estimate of the source trajectory even in the case of a single, very slow receive platform. The engineering developments and scientific findings described in this article open up the possibility of using multiple autonomous gliders integrated into an intelligent surveillance robotic networks. These kinds of long-endurance, silent, covert, smart robots, endowed with a navigation capability sufficient for operations in restricted areas, are envisaged to play an important role in future acoustic surveillance applications. The presented developments provide also opportunities in using bottom nodes equipped with AVSs or ocean bottom seismometers for ship detection and tracking, since those latter may be cabled and may also allow real-time data fusion among sparsely distributed sensor stations.

References

[1] K. D. LePage, C. Strode, and A. Tesei, "The effectiveness of autonomous networks utilizing passive and active ASW," NATO Science and Technology Organization - Centre for Maritime Research and Experimentation, Internal Rep. CMRE-MR-2015-020, Dec. 2015.

[2] P. Stinco et al., "Passive acoustic signal processing at low frequency with a 3-D acoustic vector sensor hosted on a buoyancy glider," *IEEE J. Ocean. Eng.*, vol. 46, no. 1, pp. 283–293, Jan. 2021, doi: 10.1109/JOE.2020.2968806.

[3] A. M. Thode et al., "Displaying bioacoustic directional information from sonobuoys using "Azigrams"," *J. Acoust. Soc. Amer.*, vol. 146, no. 1, pp. 95–102, 2019, doi: 10.1121/1.5114810.

[4] P. Stinco, A. Tesei, S. Biagini, M. Micheli, G. Ferri, and K. D. LePage, "Source localization using an acoustic vector sensor hosted on a buoyancy glider," in *Proc. IEEE/MTS OCEANS Marseille*, 2019, pp. 1–5, doi: 10.1109/OCEANSE.2019.8867452.

[5] A. Tesei et al., "A buoyancy glider equipped with a tri-dimensional acoustic vector sensor for real-time underwater passive acoustic monitoring at low frequency," in *Proc. IEEE/MTS OCEANS-Marseille Conf.*, 2019, pp. 1–6, doi: 10.1109/OCEANSE.2019.8867391.

[6] A. Tesei et al., "Low-frequency passive acoustic survey of ship traffic using a glider equipped with directional sensors," in *Proc. UACE19 Int. Conf. – Greece*, 2019, pp. 677–688.

[7] P. Stinco, A. Tesei, R. Dreo, and M. Micheli, "Detection of envelope modulation and direction of arrival estimation of multiple noise sources with an acoustic vector sensor," *J. Acoust. Soc. Amer.*, vol. 149, no. 3, pp. 1596–1608, 2021.

[8] D. C. Webb, P. J. Simonetti, and C. P. Jones, "SLOCUM: An underwater glider propelled by environmental energy," *IEEE J. Ocean. Eng.*, vol. 26, no. 4, pp. 447–452, Oct. 2001, doi: 10.1109/48.972077.

[9] B. G. Ferguson, K. W. Lo, and J. D. Rodgers, "Sensing the underwater acoustic environment with a single hydrophone onboard an undersea glider," in *Proc. IEEE OCEANS'10 Conf.*, Sydney, NSW, Australia, 2010, pp. 1–5, doi: 10.1109/OCEANSSYD.2010.5603889.

[10] T. K. Chandrayadula, C. W. Miller, and J. Joseph, "Monterey bay ambient noise profiles using underwater gliders," in *Proc. Meetings Acoust. ICA2013*, Acoustical Society of America, 2013, Art. no. 070031.

[11] Y. M. Jiang, A. Alvarez, D. Cecchi, B. Garau, and M. Micheli, "In-situ acoustic received level measurements with glider based reactive behaviour," in *Proc. MTS/IEEE OCEANS -Genova*, 2015, pp. 1–6.

[12] A. Tesei et al., "Passive acoustic surveillance of surface vessels using tridimensional array on an underwater glider," in *Proc. IEEE/MTS OCEANS Conf.*, Genova, Italy, 2015, pp. 1–8.

[13] G. A. Dossot et al., "An investigation of the capabilities of a short hydrophone array towed by an ocean glider," *J. Acoust. Soc. Amer.*, vol. 122, no. 5, pp. 3009–3013, 2007.

[14] J. Gebbie, M. Siderius, P. L. Nielsen, J. H. Miller, S. Crocker, and J. Giard, "Small boat localization using adaptive three-dimensional beamforming on a tetrahedral and vertical line array," in *Proc. Meetings Acoust. ICA*, 2013, Art. no. 070072.

[15] B. Armstrong, "Directional hydrophones," GeoSpectrum Technical Document 2018-464.

[16] G. L. D'Spain, J. C. Luby, G. R. Wilson, and R. A. Gramann, "Vector sensors and vector sensor line arrays: Comments on optimal array gain and detection," *J. Acoust. Soc. Amer.*, vol. 120, no. 1, pp. 171–185, Jun. 2006, doi: 10.1121/1.2207573.
[17] B. A. Cray and A. H. Nuttall, "Directivity factors for linear arrays of velocity sensors," *J. Acoust. Soc. Amer.*, vol. 110, pp. 324–331, 2001, doi: 10.1121/1.1373706.
[18] A. Nehoray and E. Paldi, "Acoustic vector-sensor array processing," *IEEE Trans. Signal Process.*, vol. 42, no. 9, pp. 2481–2491, Sep. 1994, doi: 10.1109/78.317869.
[19] F. J. Fahy, *Sound Intensity*. 2nd ed. London, U.K.: E & FN Spon, 1995.
[20] A. Trabattoni, G. Barruol, R. Dreo, A. O. Boudraa, and F. Fontaine, "Orienting and locating ocean-bottom seismometer from ship noise analysis," *Geophysical J. Int.*, vol. 220, no. 3, pp. 1774–1790, 2020. doi: 10.1093/gji/ggz519.
[21] P. P. Gandhi and S. A. Kassam, "Analysis of CFAR processors in non-homogeneous background," *IEEE Trans. Aerosp. Electron. Syst.*, vol. 24, no. 4, pp. 427–445, Jul. 1988, doi: 10.1109/7.7185.
[22] M. Ester, H. P. Kriegel, J. Sander, and X. Xu, "A density-based algorithm for discovering clusters in large spatial databases with noise," in *Proc. 2nd Int. Conf. Knowl. Discov. Data Mining*, 1996, pp. 226–231.
[23] D. A. Gershfeld and A. I. Eller, "Geometric considerations in determining the optimum frequency of acoustic propagation in a shallow water waveguide," *J. Acoust. Soc. Amer.*, vol. 78, no. 2, pp. 632–641, 1985, doi: 10.1121/1.392431.
[24] J. W. Marsh, "Sound reflection and scattering from the sea surface," *J. Acoust. Soc. Amer.*, vol. 35, no. 2, pp. 240–244, 1963.
[25] W. M. Carey, "Lloyd's mirror-image interference effects," *Acoust. Today*, vol. 5, no. 2, pp. 14–20, 2009.
[26] D. Kapolka, J. K. Wilson, J. A. Rice, and P. Hursky, "Equivalence of the waveguide invariant and two path ray theory methods for range prediction based on Lloyd's mirror patterns," in *Proc. ASA Meetings Acoust. 155*, vol. 4, 2008, Art. no. 070002, doi: 10.1121/1.2979233.
[27] J. C. Hassab, "Passive tracking of a moving source by a single observer in shallow water," *J. Sound Vib.*, vol. 44, no. 1, pp. 127–145, 1976, doi: 10.1016/0022-460X(76)90712-4.
[28] J. Hassab, "Contact localization and motion analysis in the ocean environment: A perspective," *IEEE J. Ocean. Eng.*, vol. 8, no. 3, pp. 136–147, Jul. 1983, doi: 10.1109/JOE.1983.1145559.
[29] A. M. Noll, "Short-time spectrum and 'cepstrum' techniques for vocal-pitch detection," *J. Acoust. Soc. Amer.*, vol. 36, no. 2, pp. 296–302, 1964, doi: 10.1121/1.1918949.
[30] A. V. Oppenheim and R. W. Schafer, "From frequency to quefrency: A history of the cepstrum," *IEEE Signal Process. Mag.*, vol. 21, no. 5, pp. 95–106, Sep. 2004, doi: 10.1109/MSP.2004.1328092.
[31] E. L. Ferguson, S. B. Williams, and C. T. Jin, "Improved multipath time delay estimation using cepstrum subtraction," in *Proc. IEEE Int. Conf. Acoust., Speech Signal Process.*, 2019, pp. 551–555, doi: 10.1109/ICASSP.2019.8683176.
[32] D. E. Kruse and K. W. Ferrara, "A new high resolution color flow system using an eigendecomposition-based adaptive filter for clutter rejection," *IEEE Trans. Ultrason. Ferroelect. Freq. Control*, vol. 49, no. 10, pp. 1384–1399, Oct. 2002, doi: 10.1109/TUFFC.2002.1041080.
[33] Y. Gao, "Power cepstra measured in shallow water environments," in *Proc. IEEE OCEANS'13 Conf.*, Bergem, Norway, 2013, pp. 1–7, doi: 10.1109/OCEANS-Bergen.2013.6608044.

Richard Dreo is currently a Scientist interested in passive acoustics and signal processing. He is a former Submariner of the French Navy, where he was specialized in passive acoustics and ship recognition. From 2017 to 2019, he was a Research Engineer with the French Naval Academy Research Institute, Brest, France, working on whale and ship detection with ocean-bottom seismometers. From 2019 to 2021, he joined the ASW team, NATO STO CMRE, La Spezia, Italy, as a Visiting Scientist to work on real-time detection of ships using acoustic vector sensors embedded on gliders. He is currently a Scientific Consultant in passive acoustics, mainly focusing on bio-acoustics, ship detection, and environment monitoring.

Alister Trabattoni was born in Paris, France, in 1991. He received the M.E. degree in engineering from the Ecole Centrale Paris, Paris, France, in 2016, and the Ph.D. degree in earth science from the Institut de Physique du Globe de Paris (IPGP), Paris, France, in 2020.

In 2021, he integrated (as a Postdoc) an international team gathering l'Ecole Supérieur d'Electronique de l'Ouest (ESEO), Angers, France; Università degli Studi Frederico Secondo (UNINA), Naples, Italy; and Université d'Angers (UA), Angers, France. He has been a Postdoc with Geoazur, Valbonne, France, since 2022. His main areas of research interest are distributed acoustic sensing and ocean-bottom seismology.

Pietro Stinco received the M.Sc. degree in telecommunication engineering and the Ph.D. degree in remote sensing from the University of Pisa, Pisa, Italy, in 2007 and 2010, respectively.

He is currently a Research Scientist with NATO STO CMRE, La Spezia, Italy, where his interests are in signal processing, array processing, and machine learning for ASW with autonomous underwater platforms. He was a member of NATO SET 207 on Passive Radars and of NATO SET 227 on Cognitive Radars. Before joining the NATO STO CMRE in 2016, he was a Research Associate with the Department of Information Engineering, University of Pisa.

Michele Micheli received the M.Sc. degree in telecommunication engineering and the second-level University Master's degree in underwater electroacoustic and applications from the University of Pisa, Pisa, Italy, in 2002 and 2005, respectively.

He is a Principal Technician with NATO STO CMRE, La Spezia, Italy. He is working in the field of sonar signal processing and robotics mainly for the Anti-Submarine Warfare program.

Mr. Micheli is the recipient of the NATO STO Scientific Achievement Award, as "Member of the CMRE Glider Team" in 2014 and for the "Development and Demonstration of Networked Autonomous ASW" in 2017.

Alessandra Tesei received the Ph.D. degree in telecommunications from the University of Genoa, Genoa, Italy, in 1996.

In 1996, she joined NATO STO CMRE, La Spezia, Italy, where she was involved in theoretical and experimental projects in the fields of mine hunting and port protection. Between 2010 and 2013, she was a Scientific Consultant. Since 2014, she has been again with CMRE, working as a Project Leader and as a Senior Scientist in passive and active sonar for target detection, classification, and localization by using autonomous underwater platforms. Her major research interests are in acoustic signal processing, underwater and structural acoustics, and underwater autonomous vehicles.